Stabilizing microsized Sn anodes for Na-ion batteries with extended ether electrolyte chemistry

Xiaoqiong Du, [‡] Yao Gao, [‡] Zhen Hou, Xuyun Guo, Ye Zhu, Biao Zhang*

Department of Applied Physics, Research Institute for Smart Energy, The Hong Kong Polytechnic University, Hung Hom, Hong Kong, China

Abstract

Electrolytes using ether solvents show great advantages in building robust solid electrolyte interphases (SEIs), which play a pivotal role in stabilizing alloy anodes in Na-ion batteries. Herein, we deviate from the most widely adopted methyl glymes (represented by monoglyme) to enrich the ether-based electrolyte chemistry. Stable cycling of Sn microparticles is realized in two electrolytes derived from the linear ethylene glycol diethyl ether (ethyl glyme, EGDEE) and cyclic ether (tetrahydrofuran, THF). We reveal that the formation of thin yet strong SEIs accounts for ameliorated stability and excellent rate capability. The inorganic species in the as-constructed SEIs have low crystallinity and are uniformly distributed among the organic matrix, rendering superb mechanical properties in accommodating the deformation upon sodiation, as confirmed by nano-indentation tests. This study opens the door to exploring large ether family besides the methyl glymes, and the unraveled mechanics/microstructure correlation of SEIs can help screen the potential candidates.

Introduction

The past decade has witnessed the fast development of Na-ion batteries (NIBs).[1-3] Thanks to the advantages in sustainability and cost, NIBs have been considered as attractive alternatives to Li-ion batteries (LIBs) in large-scale energy storage.[4-5] The great success in designing high-capacity cathodes such as layered oxides and polyanionic compounds promises the construction of high-energy NIBs, provided equal prominent anodes are available.[6-9] Currently, hard carbon materials are the most widely adopted anodes in NIBs.[10-12] They deliver a typical capacity of 300 mAh g^{-1}, which is much lower than the practical capacity of graphite anode in LIBs.[13-14] Moreover, the hard carbon has a lower tap density due to the presence of nanopores, deteriorating the volumetric energy density of NIBs.[15] To overcome the drawbacks of hard carbon, considerable efforts have been devoted to alloy anodes with superior theoretical capacities.[16-17] Among them, Sn anodes are of particular interest because of the high theoretical capacity of 847 mAh g^{-1} and appropriate potential (~0.20 V *vs.* Na$^+$/Na). Nevertheless, the applications of Sn anodes are afflicted by severe structural degradation due to the significant volume change (up to 420%) during the sodiation process.[18] Nanostructure design has been extensively explored in Sn anodes by anchoring nanosized Sn particles to a variety of carbon hosts.[19-26] Although significant improvement in the cyclic life has been observed, it also brings about other issues, such as large initial irreversible capacities and decreases in the density and capacity.[27]

Fortunately, recent progress suggests the microsized particles could be stabilized through interphasial engineering which is induced by electrolyte chemistry.[28-32] Our previous work also achieves long-term cyclic stability of Sn microparticles in ether-based electrolytes, owing to the possible construction of robust solid electrolyte interphase (SEI).[33] The electrolyte-mediated strategy has been generalized to other alloys anodes, such as Bi and Sb microparticles for improving cyclic stability without resorting to nanostructure design.[34-38] The success of stabilization reckons on the formation of magic SEIs by utilizing ether solvents in the electrolytes.[39-40] The oligomers arising from the reduction of ether solvents constitute the organic components in the SEI, which is supposed to possess excellent elasticity for accommodating the large deformation during the charge/discharge processes.[41] The ideal SEI layer effectively encapsulates the alloy anodes and avoids the isolation of fractured particles to maintain structural integrity. Until now, most of the works focus on the ethylene glycol dimethyl ether solvent (DME, or monoglyme), which has a low viscosity for realizing high-rate performance.[42-44] The application of DME-based electrolyte could be traced back to the 1970s when the first generation Li batteries was developed, but it was abandoned later due to oxidative decomposition on the cathode side and low boiling point.[45] The obstacle could be partly resolved by increasing the chain length of the molecular by utilizing diglyme (diethylene glycol dimethyl ether) and triglyme (triethylene glycol dimethyl ether), albeit at the expense of ionic conductivity owing to the escalated viscosity.[46-48]

However, there is a large group of candidates in the ether family. Exploring other ether solvents can open up new avenues in designing robust SEI for alloy anodes. Here, we report two new ether-based electrolytes rooted in the linear (ethylene glycol diethyl ether, EGDEE) and cyclic ether (tetrahydrofuran, THF). Both of them enable the stable cycling of microsized Sn

anodes in NIBs, which can maintain a high capacity of 647 and 766 mAh g^{-1} after 100 cycles under 0.2 A g^{-1} for EGDEE and THF-based electrolytes, respectively. The improved cyclic stability is closely related to the ultrathin (~3nm) but robust SEIs which have low crystallinity and high fluorine content. Furthermore, Young's modulus and yield strain of the SEIs constructed in different electrolytes are examined to reveal the mechanical origin for the enhanced cycling performance.

Experimental Section

Preparation of Sn/SbSn electrodes and electrolytes

Sn (Sigma-Aldrich, 10 μm, 99% trace metals basis) and Sb (Sigma-Aldrich, 100 mesh, 99.5%) powder were directly used without any purification. SbSn was synthesized by high-energy ball milling (HEBM, SPEX 8000M) method. The Sn and Sb powder with molar ratio of 1:1 (total about 2 g) was sealed in the HEBM tank (100 mL) under Ar atmosphere. The HEBM treatment was conducted for 2 hours in total with 10 min rest for every half hour. Sn or SbSn powder (70 wt.%), super P (10 wt.%), carboxymethyl cellulose (CMC, 10 wt.%), and vapor grown carbon fiber (VGCF, 10 wt.%) were mixed by planetary ball milling (QM-3SP2 planetary ball mill) for 1 hour with the weight ratio of total powder (500 mg) to stainless balls at 1:30. The ball milled powder and deionized (DI) water were mixed to uniform slurry by hand grinding and cast on the Cu foil. The conductive carbon electrodes are composed of super P or VGCF (90 wt.%) and CMC (10 wt.%). The tape was dried at 80 ˚C under vacuum and punched into electrodes with 12 mm diameter, and the mass loading of the active material was about 1 mg cm^{-2}. The neat Sn electrodes for atomic force microscopy (AFM) measurement were prepared by magnetron sputtering on Cu foil. The distance between the Sn target and Cu foil was 10 cm, and the time for sputtering was 5 min at 50 W. The sodium hexafluorophosphate ($NaPF_6$) was purchased from

Kishida Chemical co., ltd, Japan and propylene carbonate (PC) was from DoDo Chem. Fluoroethylene carbonate (FEC), ethylene glycol diethyl ether (EGDEE) and tetrahydrofuran (THF) were provided by Macklin Inc. 1M $NaPF_6$ in PC with 3 vol.% FEC (denote as 1M $NaPF_6$/PC-FEC), 1M $NaPF_6$ in EGDEE (denote as 1M $NaPF_6$/EGDEE) and 1M $NaPF_6$ in THF (denote as 1M $NaPF_6$/THF) were adopted as electrolytes.

Electrochemical performances measurement

The batteries were assembled in Ar filled glove box (O_2<0.1ppm, H_2O<0.1ppm) using CR2032 type batteries case. A piece of glass fibre (GF/D, Whatman) was used as the separator. Metallic sodium was used as a counter electrode with adding 70 uL of electrolyte per cell. The galvanostatic discharge-charge was tested on LAND battery testing system. The batteries were pre-cycled three times under 0.05 A g^{-1} to construct SEIs before long-term testing. The specific capacity is calculated based on the weight of Sn and the capacity contribution of super P and VGCF are removed from the total capacity. The capacities at increasing rates are collected on the fifth cycle. The cyclic voltammetry (CV) curves are performed on Solartron Analytical 1400 electrochemical workstation at a scan rate of 0.05 mV s^{-1} between 0-1.0 V. The electrochemical impedance spectroscopy (EIS) was collected by Biologic SP150 electrochemical workstation between 100 kHz and 0.1 Hz with an amplitude of 5 mV. Linear sweep voltammetry (LSV) was performed on Biologic SP150 electrochemical workstation with high purity Al foil as working electrodes under scan rate of 5mV s^{-1}.

Sample characterizations

The morphologies of Sn electrodes before and after cycling were investigated by scanning electron microscope (SEM, Tescan VEGA3). The nanostructures of the SEIs were examined by transmission electron microscopy (TEM, JEOL JEM-2100F) with an operating voltage of 200

kV. The fully discharged and charged samples were sealed in Rigaku *in situ* X-ray diffraction (XRD) batteries cell with a Be window to avoid the air exposure, and the XRD patterns were collected on X-ray Diffractometer (Rigaku SmartLab, 9kW). The chemical compositions of the SEIs were studied by X-ray photoelectron spectroscopy (XPS, Thermo Scientific Nexsa) using a vacuum transfer holder to avoid exposure to the air.

AFM measurements

The mechanical properties of the SEIs were conducted on the Bruker Dimension Icon AFM in an Ar filled glovebox. The neat Sn electrodes were pre-cycled two times to build SEIs. They are disassembled in the glovebox and washed with the corresponding solvent. ACTA-20 (APPNANO) was used as a probe for AFM testing. The spring constant of the probe was calculated as 20.0 N m^{-1} by the Sedar method. The deflection sensitivity was calibrated on a sapphire sample. The tip radius R (26.2 nm) was measured on the Polycarbonate sample with Young's modulus known as 2.4 GPa. Peak Force Quantitative Nanoscale Mechanical Characterization mode was adopted for the two-step test at the same position. Firstly, a small force of 30 nN was applied to trigger the elastic deformation of SEIs. A large force (up to 900 nN) is used to intentionally break the SEI for measuring the yield strain. Detailed analysis method of AFM data could be found in the previous report.[49] Briefly, the maximum elastic deformation energy (U) is used to determine the mechanical stability, which is calculated as follows:

$$U = \frac{8}{15}\left(\frac{4}{5}\pi\right)^5 \cdot r^3 \cdot (1-v^2)^4 \cdot E \cdot (\varepsilon_Y)^5 \quad \text{(Equation 1)}$$

where r is the radius of the rigid indenter (assumed as 1 μm), the ν is the SEI Poisson's ratio, and a typical value of 0.3 is used, E and ε_Y are corrected Young's modulus and yield strain by eliminating the substrate's interference.

Results and discussion

We deviate from the classic DME groups to explore novel ether electrolyte chemistry. The linear ether EGDEE and cyclic ether THF are first adopted for designing SEIs in NIBs. As illustrated in **Scheme 1**, EGDEE resembles the structure of DME by replacing the terminal methyl group with the ethyl group. Such a modification dramatically improves the boiling point from 85 ºC to 121 ºC to benefit battery safety. Differing from the linear EGDEE, the THF is a cyclic ether for offering an opportunity in the cyclic structured solvent, similar to ethylene carbonate (EC) in ester electrolyte that is indispensable in commercial electrolyte formulation, although the high vapour pressure would be a problem in practical application. The electrochemical stability of sodium electrolytes with ether solvents are investigated by linear sweep voltammetry (LSV) using high purity Al foil as a cathode (**Figure S1**). The DME-based electrolyte shows more severe electrolyte decomposition than the EGDEE and THF ones when the voltage reaches 4.5V in the first scan (**Figure S1a**). In the following scans, the oxidation voltages of EGDEE and THF-based electrolytes can be estimated at 4.75 V thanks to the formation of cathode electrolyte interphases (CEIs), which are much chemically stable than DME counterparts (**Figure S1b and c**).
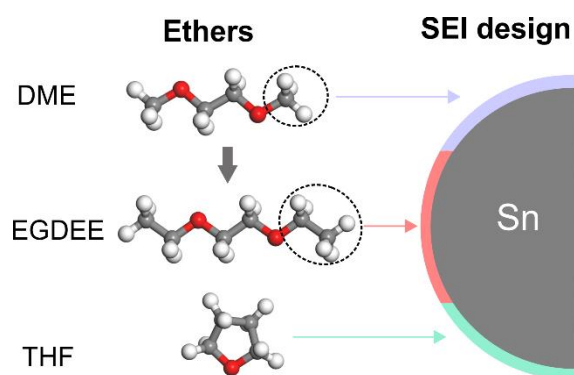
Scheme 1 Chemical structures of DME, EGDEE and THF ethers and the SEI design.

The electrochemical performances of microsized Sn electrodes (~1.02 um, **Figure S2)** adopting conventional carbonate-based electrolytes (1M NaPF$_6$/PC-FEC) and ether-based electrolytes (1M NaPF$_6$/EGDEE and 1M NaPF$_6$/THF) are compared in **Figure 1**. High initial Coulombic efficiencies (ICEs) of 83.5%, 83.3% and 85.5% are achieved for these three electrolytes, which are ascribed to the large particles of Sn electrodes that can dramatically reduce the active interfaces with the electrolyte. As widely observed previously, FEC additive is ineffective to protect the microsized Sn particles, it shows rapid capacity degradation in the 5th cycle (**Figure 1a**) with 1M NaPF$_6$/PC-FEC electrolyte.[50-51] In sharp contrast, the Sn electrodes exhibit significantly improved stability in EGDEE and THF-based electrolytes. **Figure 1b and c** present discharge-charge curves of the 1st and 5th cycles under 0.05 A g^{-1} in 1M NaPF$_6$/EGDEE and NaPF$_6$/THF, showing a high initial reversible capacity of 734 and 760 mAh g^{-1} respectively. The capacity contribution of super P and VGCF are evaluated and removed from the total capacity, which display low capacities of about 100 and 20 mAh g^{-1}, respectively (**Figure S3 and S4**). The clear plateaus indicate the multi-step Na alloying mechanisms. In cyclic voltammetry (CV) measurements (**Figure S5**), take Sn electrode in 1M NaPF$_6$/EGDEE (**Figure S5b**) as an example, four peaks located at 0.37, 0.19, 0.12, and 0.007 V in the cathodic scan are observed, corresponding respectively to the formation of Na$_x$Sn (x<1), NaSn, Na$_9$Sn$_4$, and Na$_{15}$Sn$_4$ phases.[33] As to the anodic scans, four peaks at 0.24, 0.28, 0.55, and 0.67 V are matched with their de-alloying processes. The *ex situ* X-ray diffraction (XRD) patterns (**Figure S6**) of Sn electrodes discharged to 0 V confirm the Na-rich phases of Na$_9$Sn$_4$ and Na$_{15}$Sn$_4$, in agreement with the alloying of around 3.4 Na ion per Sn as inferred from the reversible capacity. The co-existence of Na$_9$Sn$_4$ may be originated from the incomplete sodiation reactions of the bulk Sn microparticles. Nearly pure Sn phase is detected upon charging, suggesting the highly reversible

alloying/de-alloying processes for microsized Sn electrodes in NIBs. Moreover, the phase transformation pathways are not altered with the electrolytes.
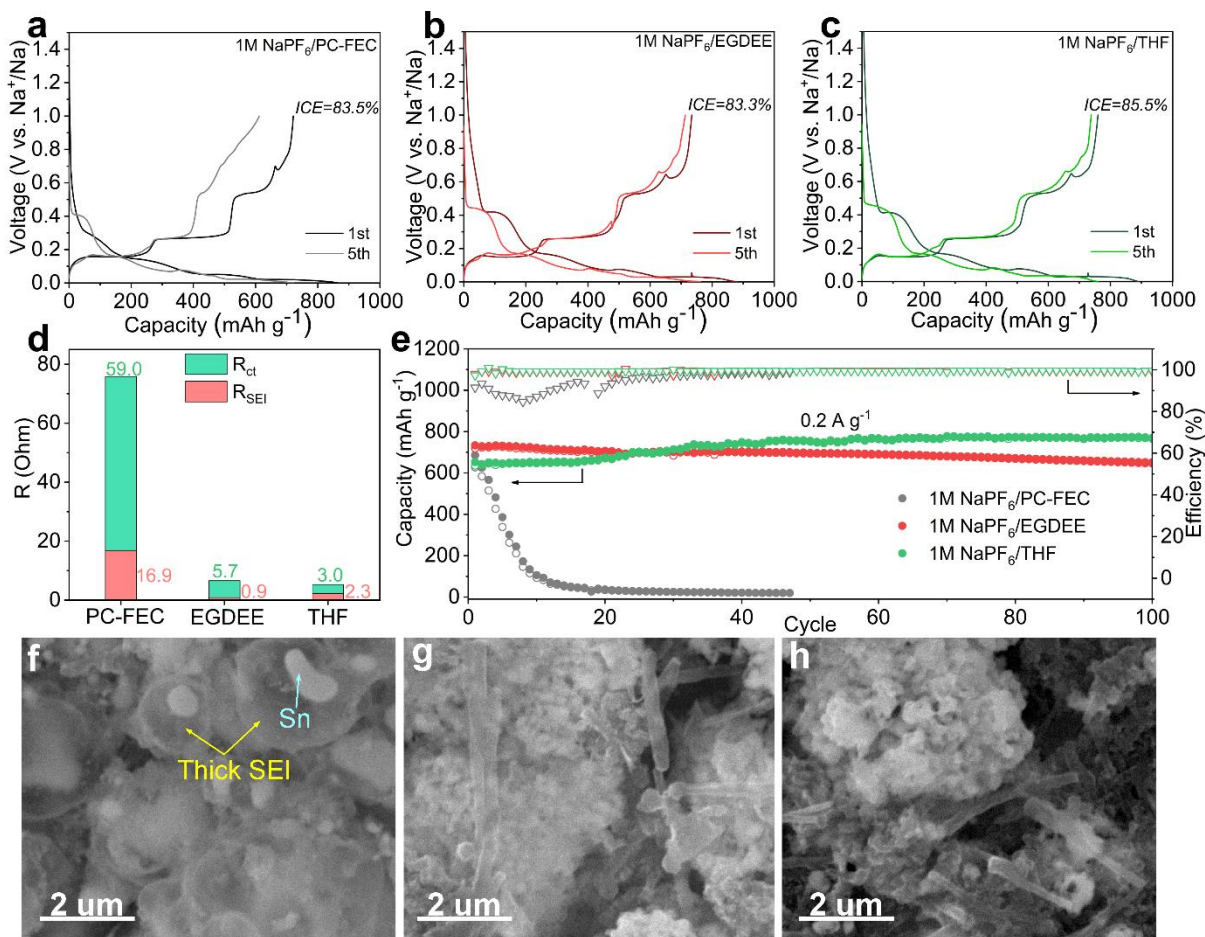

Figure 1 The selected galvanostatic discharge-charge profiles of Sn electrodes in a) 1M NaPF$_6$/PC-FEC, b) 1M NaPF$_6$/EGDEE and c) 1M NaPF$_6$/THF electrolytes under 0.05 A g^{-1}. d) the fitted resistances values of Sn electrodes after cycling three times; e) cycling performance under 0.2 A g^{-1}; SEM images of Sn electrodes in: f) 1M NaPF$_6$/PC-FEC; g) 1M NaPF$_6$/EGDEE and h) 1M NaPF$_6$/THF after 100 cycles.

The electrochemical impedance spectroscopy spectra (EIS) of the electrodes after constructing SEIs through pre-cycling three times are examined (**Figure S7**). The equivalent circuited fitted results indicate that both the SEIs (R$_{SEI}$) and charge transfer (R$_{ct}$) resistances are much lower in

EGDEE and THF electrolytes than in PC-FEC counterparts (**Figure 1d**). More importantly, Sn

electrodes show stable cyclic performances with approximately 90% and 100% capacity

retention after 100 cycles in 1M $NaPF_6$/EGDEE and 1M $NaPF_6$/THF electrolytes under 0.2 A g^{-1}

(**Figure 1e**). The high average CEs over 99.3% in ether-based electrolytes indicate negligible

parasitic reactions between the electrodes and the electrolytes after several initial cycles. In

comparison, the CE continuously decreases to 84.6% and capacity fast decays to 0 in 1M

$NaPF_6$/PC-FEC electrolyte, suggesting that the bulk materials constantly break and produce new

SEI during the cyclic measurements. Such deterioration could not be alleviated by decreasing the

current density: similar degradation is found when cycled at a low rate of 0.05 A g^{-1} (**Figure S8**).

To investigate the surface morphologies of Sn electrodes with the three electrolytes after long-

term cycling, the scanning electron microscope (SEM) is performed. Obvious crakes are

observed in the electrodes cycled under all three electrolytes due possibly to repeated

expansion/contraction (**Figure S9**) and escaping of the solvents. Thick SEI layers that wrap the

Sn particles could be discerned for the electrode tested in 1M $NaPF_6$/PC-FEC, as reflected by the

apparent boundary between SEI and Sn particles (**Figure 1f**). The observation indicates the

copious electrolyte decomposition that results in continuous SEI growth, which agrees well with

the low CE. In contrast to it, the surface of active particles after cycling in EGDEE and THF-

based electrolytes is smooth and uniform under the resolution of SEM (**Figure 1g and h**), due

potentially to the formation of thin and conformal SEI layer as will be confirmed by the high-

resolution transmission microscopy (HRTEM). Besides, the thickness changes of the electrodes

with EGDEE-based electrolyte are also investigated to understand the electrochemical stability.

As shown in **Figure S10**, a periodic expansion and contraction of the electrodes are observed for

the first two cycles. Although it shows significant thickness increase during sodiated states, it can

be well recuperated at fully desodiated states, suggesting the good affordability of the electrodes to withstand volume change in ether-based electrolytes. The rate performances are evaluated in **Figure 2**. The Sn electrodes exhibit superior rate capabilities, delivering considerable capacities of 712.3/737.9, 641.7/670.1, 570.4/604.3, 476.8/536.3, 396.7/450.6 and 412.4/384.8 mAh g^{-1} for EGDEE and THF-based electrolytes with current density increases from 0.05 to 1 A g^{-1}. Moreover, high reversible capacities of 385.5 and 523.1 mAh g^{-1} with the capacity retention of 95.5 and 100% are maintained under 1A g^{-1} over 200 cycles with 1M NaPF$_6$/EGDEE and 1M NaPF$_6$/THF electrolytes (**Figure S11**), respectively, demonstrating the enhanced stabilities and fast kinetics of Sn microparticles with these two ether-based electrolytes.
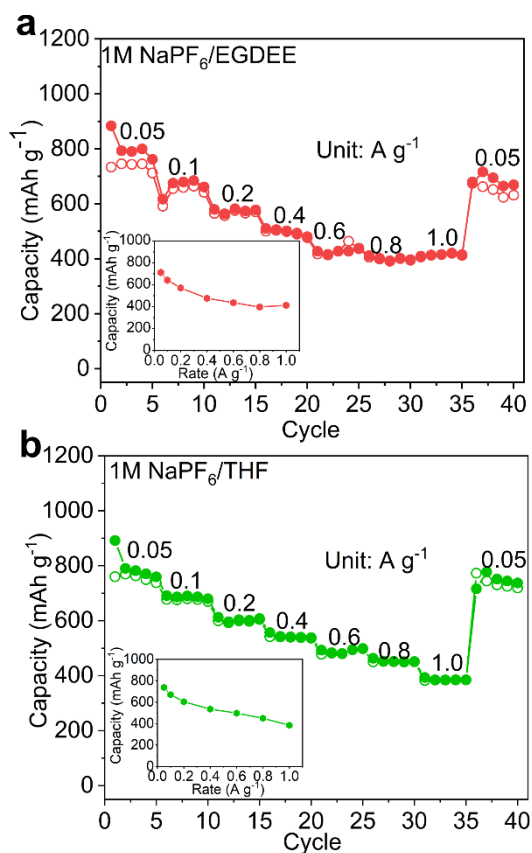

Figure 2 Rate performance of Sn electrodes in a) 1M NaPF$_6$/EGDEE and b) 1M NaPF$_6$/THF.

The above results demonstrate the essential roles of SEIs in stabilizing microsized Sn anodes. The nanostructures of SEIs in the three electrolytes are examined by TEM to investigate the

underlying mechanism. It is found that the Sn particles after three cycles are not fully broken to small pieces but still maintain the microsized morphologies (**Figure S12**). Specifically, in 1M $NaPF_6$/PC-FEC electrolyte, a heterogeneous SEI with a thickness of about 25.2 nm is formed **(Figure 3a and b)**. Some tiny crystals are present in the SEI, and their lattice structure is analyzed by the HRTEM (**Figure 3c**). One pair of crossed lattices of 2.6 Å and 1.6 Å can be assigned to Na_2CO_3 species on the (11-2) and (-422) planes (COD#9009418), respectively. The d-spacing of 2.3 Å might be the (002) plane of NaF (PDF#73-1922). Turning to the SEI in 1M $NaPF_6$/EGDEE electrolyte (**Figure 3e-g**), it exhibits ultrathin (about 2.4 nm) and amorphous morphologies without showing any crystalline particles. The SEI established in 1M $NaPF_6$/THF shows similar nanostructures to that in 1M $NaPF_6$/EGDEE, where thin (about 2.4 nm) and amorphous SEI uniformly adheres to the Sn particles (**Figure 3i-k**). Due to the chelation behaviour of cation and linear ether molecules, the EGDEE-based electrolyte is more stable against reduction than THF counterpart, which may lead to the thinner SEI in former electrolyte; while the carbonate solvents which are less resistant against the electrochemical reductions than the ether solvents are inclined to generate thicker SEI.[52-53] Moreover, the thin SEI layer is ascribed to the effective suppression of continuous electrolyte decomposition, which can avoid the over-growth of interphases and lead to the small thickness.[39] Meanwhile, the thin SEI restricts the crystallization of the inorganic species, resulting in amorphous morphologies.[54-55] Besides, **Figure 3g and k** show the Sn lattices with high crystallinity after cycling, indicating Na_xSn recovers to Sn upon charging, which supports the *ex situ* XRD results. The nanostructures of SEIs in both linear and cyclic ether-based electrolytes differ significantly from the one in classic carbonate electrolyte, as illustrated by **Figure 3d, h and l**. In general, the SEI could be treated as a composite with the inorganic species distributed among the organic matrixes. The

relatively large inorganic particles with high crystallinity are presented in the SEI with carbonate electrolyte, which may deteriorate the mechanical resilience. Furthermore, the thick SEI is detrimental to the Na ion transfer and undermines the rate capability.
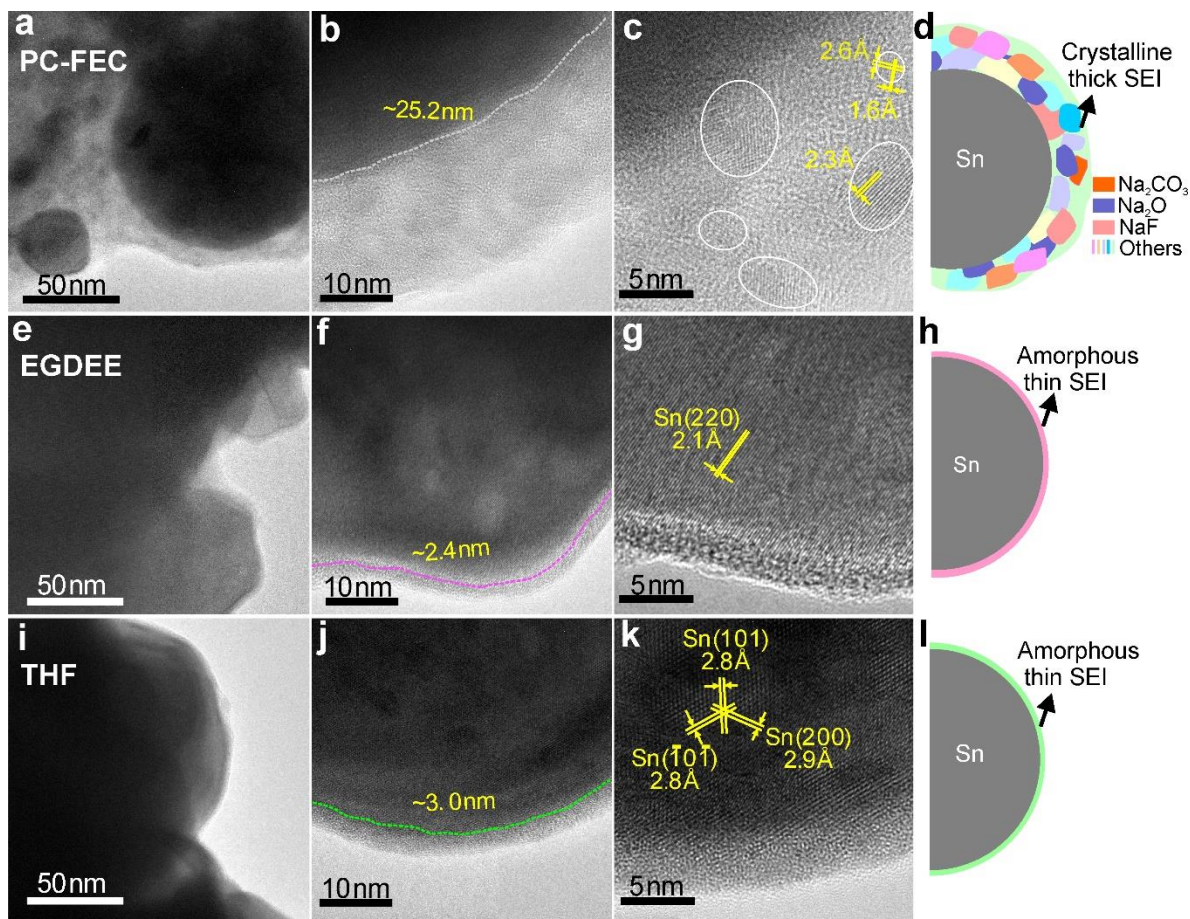

Figure 3 TEM/HRTEM images and SEI illustrations of Sn electrodes after three cycles in a-d) 1M $NaPF_6$/PC-FEC, e-h) 1M $NaPF_6$/EGDEE and i-l) $NaPF_6$/THF electrolytes.

To analyze the chemical compositions of the distinct SEIs constructed in the three electrolytes, X-ray photoelectron spectroscopy (XPS) measurements are conducted for the Sn electrodes after cycling three times. Similar species are detected in the three SEIs but with massive differences in the relative amounts due to the possible different decomposition paths of these three electrolytes (Equation S1-S10). In C1s spectra of all the electrolytes (**Figure 4a**), the deconvoluted peaks

located at 284.5, 285.4, 286.1, and 287.4 eV can be assigned to organic carbonates of C-C/C-H, C-O, O-C-O, and C=O species, which are mainly originated from the decomposition of PC, FEC, EGDEE and THF.[56-57] In particular, the Na_2CO_3 species is defined at 289.5 eV.[58] As for the O1s spectra presented in **Figure 4b**, the peaks at 532.3 and 533.3 eV can be ascribed to the organic ingredients of O-C=O and C-O, consistent with that in C1s spectra.[59] Additionally, Na-O bonding at 531.5 eV is derived from the sodium alkyl carbonates (R-OCO$_2$Na), Na_2CO_3 or Na_2O species.[60] We also examine the detailed F1s spectra considering the pivotal roles of F-related species.[61-62] Two pronounced peaks of Na-F (684.9 eV) and P-F (687.7 eV) bonding (**Figure 4c**) correspond respectively to the salt decomposition products of NaF and Na_xPF_y or Na_xPO_yF.[63] To compare the degree of electrolyte decomposition in carbonate and ether-based electrolytes, the atomic concentration in the survey spectrum is plotted in **Figure S13**, where the contents of inorganic Na_2CO_3, Na-O, and Na-F species are quantified according to the peak area in the C, O, and F spectra. Although C-O, C=O and Na-O species from CMC binder may also present, Na_2CO_3 and Na-O components are enriched in carbonate electrolyte-derived SEI (**Figure S13a and b**), which agrees with the TEM observations. Among these two ether-based electrolytes, higher Na_2CO_3 and Na-O species are observed for THF-based electrolyte, for the ring structure of the cyclic ether solvent molecules are vulnerable to be decomposed during the cycling. However, much higher Na-F species could be found under ether-based SEI compared to the carbonate counterpart (**Figure S13c**). The fluorinated SEI is reported to possess enhanced ionic conductivity and excellent mechanical and electrochemical stability for maintaining the structural integrity.[62, 64]
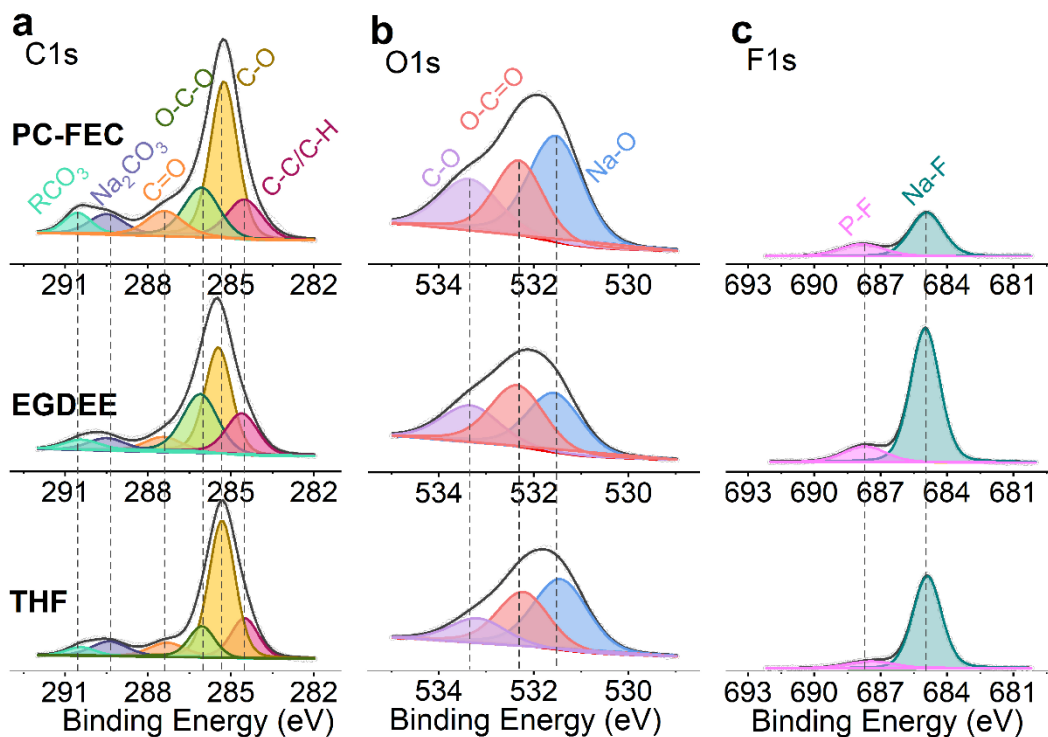
Figure 4 XPS measurements of a) C1s, b) O1s and c) F1s for cycled Sn electrodes in corresponding electrolytes.

The disclosed SEI nanostructure has a significant impact on the electrochemical performance of Sn micro-particles. It is speculated that the ether-derived SEIs hold great advantages in accommodating the deformation, but direct evidence lacks. We employed atomic force microscopy (AFM) to probe the mechanical properties of SEIs formed in different electrolytes. To exclude the potential interferences from the binder and conductive carbon, neat Sn electrodes are prepared by magnetron sputtering. Similarly, the neat Sn electrodes are pre-cycled in the three electrolytes to build SEIs for AFM tests, which show identical voltages profiles as observed for the conventional electrode (**Figure S14**). The surface flatness of the electrodes is investigated by AFM topography measurements (**Figure S15**). Compared with the pristine electrodes, the surface roughness (Ra) decreases after cycling in ether-based electrolytes while

15

increases in PC-FEC electrolyte, suggesting the severe electrode deterioration in the latter (**Table S1**). A two-step AFM test is conducted to explore the elastic and plastic deformation behaviour of SEIs (**Figure 5a inset**). To increase the accuracy, the tests are conducted in at least 80 different positions to calculate the average value. **Figure 5a** presents the typical force curves at the same point obtained from the first and second steps of AFM test, respectively. Young's modulus (E) is calculated from the first test that is conducted in the elastic deformation region, while the yield strain (ε_Y) of SEIs is determined in the second test where a large force is applied to break the SEI deliberately. The results show that the SEI formed in 1M $NaPF_6$/PC-FEC has a high average E of 280.5 MPa, compared to 244.7 MPa and 183.4 MPa for the ones constructed in EGDEE and THF-derived electrolytes, respectively (**Figure 5b**). This observation is ascribed to the better crystallinity and high contents of inorganic species in the SEI built with 1M $NaPF_6$/PC-FEC electrolyte. The high crystalline inorganic particles would have much higher Young's modulus than the amorphous components.[65] Nevertheless, the SEI in ether-based electrolytes shows excellent elasticity, evidenced by the large ε_Y of 0.38 and 0.41 for the ones formed respectively in 1M $NaPF_6$/EGDEE and 1M $NaPF_6$/THF, compared to 0.32 for the SEI in carbonate electrolyte (**Figure 5b**). Both high values of E and ε_Y are beneficial to the mechanical stability of SEI subject to expansion. The recent study suggests the maximum elastic deformation energy ($U \propto E \cdot \varepsilon_Y^5$, Equation 1) reveals the combining effects of E and ε_Y in resisting the structure deformation.[49] The U distribution and the average value are given in **Figure 5c**. The U value is 56.3 and 72.0 pJ for the SEIs in EGDEE and THF-based electrolytes, respectively, outperforming the 35.8 pJ for the one in $NaPF_6$/PC-FEC. The results indicate that, although having a small thickness, the SEIs in the two ether-based electrolytes have better mechanical

stability. Such a stable SEI can effectively prevent excessive electrolyte reduction and encapsulate the active particles, thus benefiting the cyclic stability of microsized Sn electrodes.
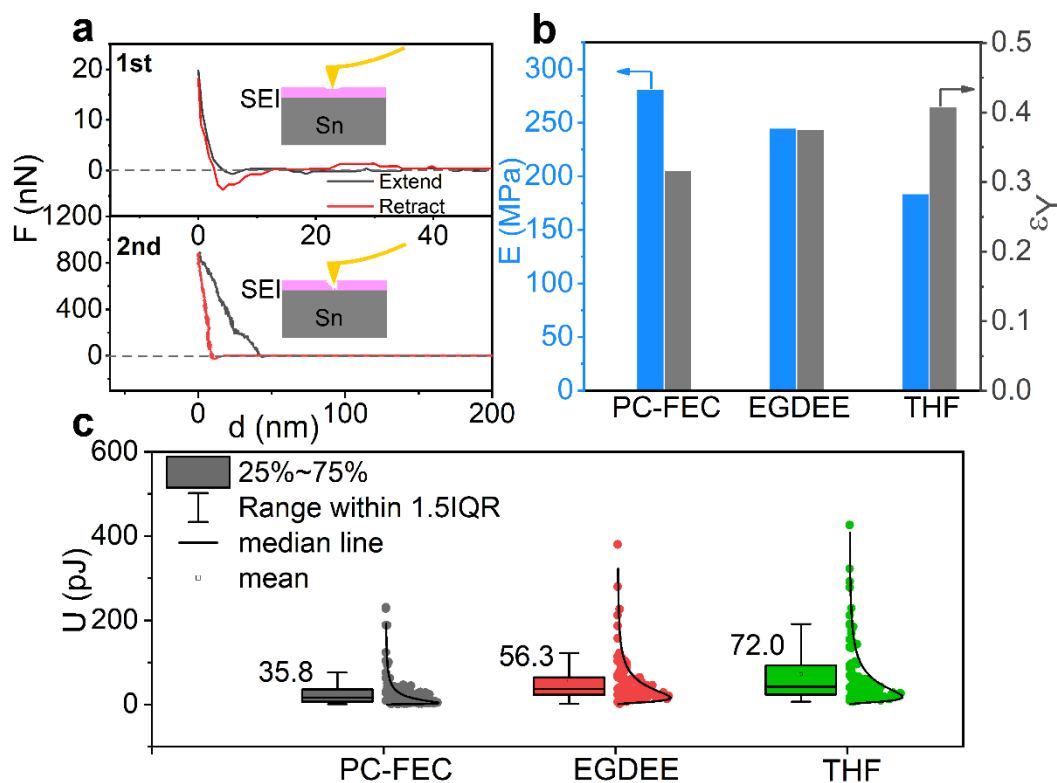

Figure 5 Mechanical properties of SEIs. a) Characteristic force curves obtained from the AFM tests on magnetron sputtered Sn electrodes (inset: the illustration of elastic and plastic deformation for the 1st and 2nd tests.); b) average Young's modulus and yield strain ε_Y and c) U for SEIs formed in the three electrolytes. Sample size = 108, 91 and 87 for 1M NaPF$_6$/PC-FEC, 1M NaPF$_6$/EGDEE and 1M NaPF$_6$/THF, respectively.

Lastly, the construction of SEI can be readily generalized to stabilizing other Sn-based alloy anodes. The SbSn phase is synthesized by high-energy ball milling of commercial Sn and Sb powder. The XRD of the synthesized SbSn is presented in **Figure S16a**, agreeing well with the SbSn standard pattern (PDF#33-0118). The SbSn sample has an average particle size of 2.05 um (**Figure S16b**). The electrochemical performances of SbSn electrodes are tested between 0-1.5 V

in 1M NaPF$_6$/EGDEE and 1M NaPF$_6$/THF electrolytes. As shown in **Figure S17**, high ICEs of 83.9% and 83.7% are realized in 1M NaPF$_6$/EGDEE and 1M NaPF$_6$/THF, respectively, owing to restricted SEI formation on the SbSn microparticles with low surface area. The long-term cyclic performances are evaluated under 0.2 A g^{-1}. High capacities of 582.3 and 507.6 mAh g^{-1} are maintained after 100 cycles in EGDEE and THF-based electrolytes. The observations confirm the critical roles of SEI in stabilizing microsized alloy anodes and the advantages of EGDEE and THF solvents in building robust SEI. The reasons for the enhanced electrochemical performances of the Sn-based alloy anodes are closed correlated to the unique SEIs. The ultra-thin SEI layers have low resistances, which are favourable to the Na ion transfer and facilitate the rate capabilities. The abundant Na-F components in the SEIs can enhance ionic conductivity and electrochemical stability of the SEI and thus keep the solidity of the electrodes. The SEIs with large maximum elastic deformation energy can accommodate the large volume expansions without pulverization during sodiation process, therefore, the long-term high capacities of the electrodes can be maintained.

Conclusions

We develop two novel electrolytes based on linear and cyclic ether, which enable the stable cycling of Sn electrodes consisting of microsized particles. The Sn electrodes show a reversible capacity of 647 and 766 mAh g^{-1} after 100 cycles in 1M NaPF$_6$/EGDEE and 1M NaPF$_6$/THF electrolytes. The enhanced electrochemical performance lies in the construction of a mechanically strong SEI. AFM tests prove the SEIs in the two ether electrolytes have higher maximum elastic deformation energy (U) than the counterpart in 1M NaPF$_6$/PC-FEC, offering superb capability in accommodating the large deformation during sodiation. To explore the microstructural origin of the enhanced stability, we unravel the unique nanostructure of SEIs by

HRTEM and XPS. It shows that, compared to the SEI in carbonate electrolytes, the ones derived in both EGDEE and THF electrolytes have smaller thickness with poorer crystallinity of inorganic species that are distributed in the organic matrix. Although such a structure diminishes Young's modulus of the SEI, it significantly heightens the yield strain for obtaining high U values. The results presented here indicate the great opportunity in building robust SEIs through ether solvent, which contains a large family of candidates besides widely adopted methyl glyme groups. The disclosed microstructure-mechanical stability correlation would benefit the screening of potential ether candidates and the rational design of SEI for stabilizing alloys anodes.

ASSOCIATED CONTENT

Supporting Information

The following files are available free of charge.

The SEM images of pristine Sn electrode and after long-term cycling, CV curves, *ex situ* XRD, rate performances, EIS, AFM topography images, surface roughness data, SEM and XRD of microsized SbSn and electrochemical performances of SbSn electrodes. (PDF)

AUTHOR INFORMATION

Corresponding Author

* Biao Zhang (biao.ap.zhang@polyu.edu.hk)

Author Contributions

‡These authors contributed equally.

ACKNOWLEDGMENT

REFERENCES

1.   Palomares, V.; Serras, P.; Villaluenga, I.; Hueso, K. B.; Carretero-González, J.; Rojo, T., Na-ion batteries, recent advances and present challenges to become low cost energy storage systems. *Energy & Environmental Science* **2012,** *5* (3), 5884-5901.
2.   Pan, H.; Hu, Y.-S.; Chen, L., Room-temperature stationary sodium-ion batteries for large-scale electric energy storage. *Energy & Environmental Science* **2013,** *6* (8), 2338-2360.
3.   Sun, J.; Lee, H. W.; Pasta, M.; Yuan, H.; Zheng, G.; Sun, Y.; Li, Y.; Cui, Y., A phosphorene-graphene hybrid material as a high-capacity anode for sodium-ion batteries. *Nat Nanotechnol* **2015,** *10* (11), 980-985.
4.   Tarascon, J.-M., Na-ion versus Li-ion batteries: complementarity rather than competitiveness. *Joule* **2020,** *4* (8), 1616-1620.
5.   Hirsh, H. S.; Li, Y.; Tan, D. H.; Zhang, M.; Zhao, E.; Meng, Y. S., Sodium-ion batteries paving the way for grid energy storage. *Advanced Energy Materials* **2020,** *10* (32), 2001274.
6.   Han, M. H.; Gonzalo, E.; Singh, G.; Rojo, T., A comprehensive review of sodium layered oxides: powerful cathodes for Na-ion batteries. *Energy & Environmental Science* **2015,** *8* (1), 81-102.
7.   Ni, Q.; Bai, Y.; Wu, F.; Wu, C., Polyanion-type electrode materials for sodium-ion batteries. *Advanced Science* **2017,** *4* (3), 1600275.
8.   Zhao, C.; Wang, Q.; Yao, Z.; Wang, J.; Sánchez-Lengeling, B.; Ding, F.; Qi, X.; Lu, Y.; Bai, X.; Li, B., Rational design of layered oxide materials for sodium-ion batteries. *Science* **2020,** *370* (6517), 708-711.
9.   Wang, Y.; Bai, P.; Li, B.; Zhao, C.; Chen, Z.; Li, M.; Su, H.; Yang, J.; Xu, Y., Ultralong Cycle Life Organic Cathode Enabled by Ether‐Based Electrolytes for Sodium‐Ion Batteries. *Advanced Energy Materials* **2021,** *11* (38), 2101972.
10.   Chen, D.; Zhang, W.; Luo, K.; Song, Y.; Zhong, Y.; Liu, Y.; Wang, G.; Zhong, B.; Wu, Z.; Guo, X., Hard carbon for sodium storage: mechanism and optimization strategies toward commercialization. *Energy & Environmental Science* **2021,** *14* (4), 2244-2262.
11.   Xiao, L.; Lu, H.; Fang, Y.; Sushko, M. L.; Cao, Y.; Ai, X.; Yang, H.; Liu, J., Low‐Defect and Low‐Porosity Hard Carbon with High Coulombic Efficiency and High Capacity for Practical Sodium Ion Battery Anode. *Advanced Energy Materials* **2018,** *8* (20), 1703238.
12.   Hou, B. H.; Wang, Y. Y.; Ning, Q. L.; Li, W. H.; Xi, X. T.; Yang, X.; Liang, H. J.; Feng, X.; Wu, X. L., Self-supporting, flexible, additive-free, and scalable hard carbon paper self-interwoven by 1D microbelts: superb room/low-temperature sodium storage and working mechanism. *Advanced Materials* **2019,** *31* (40), 1903125.
13.   Lin, X.; Du, X.; Tsui, P. S.; Huang, J.-Q.; Tan, H.; Zhang, B., Exploring room-and low-temperature performance of hard carbon material in half and full Na-ion batteries. *Electrochimica Acta* **2019,** *316*, 60-68.

14.   Bai, P.; Han, X.; He, Y.; Xiong, P.; Zhao, Y.; Sun, J.; Xu, Y., Solid electrolyte interphase manipulation towards highly stable hard carbon anodes for sodium ion batteries. *Energy Storage Materials* **2020,** *25*, 324-333.

15.   Xiao, B.; Rojo, T.; Li, X., Hard carbon as sodium-ion battery anodes: progress and challenges. *ChemSusChem* **2019,** *12* (1), 133-144.

16.   Luo, W.; Shen, F.; Bommier, C.; Zhu, H.; Ji, X.; Hu, L., Na-ion battery anodes: materials and electrochemistry. *Accounts of chemical research* **2016,** *49* (2), 231-240.

17.   Zheng, S.-M.; Tian, Y.-R.; Liu, Y.-X.; Wang, S.; Hu, C.-Q.; Wang, B.; Wang, K.-M., Alloy anodes for sodium-ion batteries. *Rare Metals* **2020**, 1-18.

18.   Tan, H.; Chen, D.; Rui, X.; Yu, Y., Peering into alloy anodes for sodium-ion batteries: current trends, challenges, and opportunities. *Advanced Functional Materials* **2019,** *29* (14), 1808745.

19.   Ying, H.; Zhang, S.; Meng, Z.; Sun, Z.; Han, W.-Q., Ultrasmall Sn nanodots embedded inside N-doped carbon microcages as high-performance lithium and sodium ion battery anodes. *Journal of Materials Chemistry A* **2017,** *5* (18), 8334-8342.

20.   Li, S.; Wang, Z.; Liu, J.; Yang, L.; Guo, Y.; Cheng, L.; Lei, M.; Wang, W., Yolk-shell Sn@C eggette-like nanostructure: application in lithium-ion and sodium-ion batteries. *ACS applied materials & interfaces* **2016,** *8* (30), 19438-19445.

21.   Mao, M.; Yan, F.; Cui, C.; Ma, J.; Zhang, M.; Wang, T.; Wang, C., Pipe-wire TiO_2-Sn@carbon nanofibers paper anodes for lithium and sodium ion batteries. *Nano letters* **2017,** *17* (6), 3830-3836.

22.   Liu, Y.; Zhang, N.; Jiao, L.; Tao, Z.; Chen, J., Ultrasmall Sn nanoparticles embedded in carbon as high-performance anode for sodium-ion batteries. *Advanced Functional Materials* **2015,** *25* (2), 214-220.

23.   Xie, X.; Kretschmer, K.; Zhang, J.; Sun, B.; Su, D.; Wang, G., Sn@CNT nanopillars grown perpendicularly on carbon paper: a novel free-standing anode for sodium ion batteries. *Nano Energy* **2015,** *13*, 208-217.

24.   Luo, L.; Song, J.; Song, L.; Zhang, H.; Bi, Y.; Liu, L.; Yin, L.; Wang, F.; Wang, G., Flexible conductive anodes based on 3D hierarchical Sn/NS-CNFs@rGO network for sodium-ion batteries. *Nano-micro letters* **2019,** *11* (1), 1-14.

25.   Palaniselvam, T.; Goktas, M.; Anothumakkool, B.; Sun, Y. N.; Schmuch, R.; Zhao, L.; Han, B. H.; Winter, M.; Adelhelm, P., Sodium storage and electrode dynamics of tin-carbon composite electrodes from bulk precursors for sodium‐ion batteries. *Advanced Functional Materials* **2019,** *29* (18), 1900790.

26.   Xu, Y.; Zhu, Y.; Liu, Y.; Wang, C., Electrochemical performance of porous carbon/tin composite anodes for sodium‐ion and lithium‐ion batteries. *Advanced Energy Materials* **2013,** *3* (1), 128-133.

27.   Zhang, Y.; Wang, Y.; Kong, D.; Yang, Y.; Wang, Y.; Guo, Y.; Lu, Y.; Kim, J.-K.; Luo, Y., In situ growth of Sn nanoparticles confined carbon-based TiO_2/TiN composite with long-term cycling stability for sodium-ion batteries. *Electrochimica Acta* **2021,** *367*, 137450.

28.   Huang, J.; Guo, X.; Du, X.; Lin, X.; Huang, J.-Q.; Tan, H.; Zhu, Y.; Zhang, B., Nanostructures of solid electrolyte interphases and their consequences for microsized Sn anodes in sodium ion batteries. *Energy & Environmental Science* **2019,** *12* (5), 1550-1557.

29.   Zhang, N.; Sun, C.; Huang, Y.; Zhu, C.; Wu, Z.; Lv, L.; Zhou, X.; Wang, X.; Xiao, X.; Fan, X.; Chen, L., Tuning electrolyte enables microsized Sn as an advanced anode for Li-ion batteries. *Journal of Materials Chemistry A* **2021,** *9* (3), 1812-1821.

30.   Jin, Y.; Xu, Y.; Le, P. M.; Vo, T. D.; Zhou, Q.; Qi, X.; Engelhard, M. H.; Matthews, B. E.; Jia, H.; Nie, Z., Highly Reversible Sodium Ion Batteries Enabled by Stable Electrolyte-Electrode Interphases. *ACS Energy Letters* **2020,** *5* (10), 3212-3220.

31.   Du, X.; Gao, Y.; Zhang, B., Building Elastic Solid Electrolyte Interphases for Stabilizing Microsized Antimony Anodes in Potassium Ion Batteries. *Advanced Functional Materials* **2021,** 2102562.

32.   Li, K.; Zhang, J.; Lin, D.; Wang, D.-W.; Li, B.; Lv, W.; Sun, S.; He, Y.-B.; Kang, F.; Yang, Q.-H., Evolution of the electrochemical interface in sodium ion batteries with ether electrolytes. *Nature communications* **2019,** *10* (1), 1-10.

33.   Zhang, B.; Rousse, G.; Foix, D.; Dugas, R.; Corte, D. A. D.; Tarascon, J. m., Microsized Sn as advanced anodes in glyme-based electrolyte for Na-Ion batteries. *Advanced Materials* **2016,** *28* (44), 9824-9830.

34.   Wang, C.; Wang, L.; Li, F.; Cheng, F.; Chen, J., Bulk bismuth as a high-capacity and ultralong cycle-life anode for sodium-ion batteries by coupling with glyme-based electrolytes. *Advanced Materials* **2017,** *29* (35), 1702212.

35.   Huang, J.; Lin, X.; Tan, H.; Zhang, B., Bismuth microparticles as advanced anodes for potassium-ion battery. *Advanced Energy Materials* **2018,** *8* (19), 1703496.

36.   Lei, K.; Wang, C.; Liu, L.; Luo, Y.; Mu, C.; Li, F.; Chen, J., A porous network of bismuth used as the anode material for high-energy-density potassium-ion batteries. *Angewandte Chemie* **2018,** *130* (17), 4777-4781.

37.   Zhang, Q.; Mao, J.; Pang, W. K.; Zheng, T.; Sencadas, V.; Chen, Y.; Liu, Y.; Guo, Z., Boosting the potassium storage performance of alloy-based anode materials via electrolyte salt chemistry. *Advanced Energy Materials* **2018,** *8* (15), 1703288.

38.   Zhou, L.; Cao, Z.; Zhang, J.; Cheng, H.; Liu, G.; Park, G. T.; Cavallo, L.; Wang, L.; Alshareef, H. N.; Sun, Y. K., Electrolyte-Mediated Stabilization of High-Capacity Micro-Sized Antimony Anodes for Potassium-Ion Batteries. *Advanced Materials* **2021,** *33* (8), 2005993.

39.   Zhang, J.; Wang, D. W.; Lv, W.; Qin, L.; Niu, S.; Zhang, S.; Cao, T.; Kang, F.; Yang, Q. H., Ethers Illume Sodium-Based Battery Chemistry: Uniqueness, Surprise, and Challenges. *Advanced Energy Materials* **2018,** *8* (26), 1801361.

40.   Li, B.; Zhao, J.; Zhang, Z.; Zhao, C.; Sun, P.; Bai, P.; Yang, J.; Zhou, Z.; Xu, Y., Electrolyte‐Regulated Solid‐Electrolyte Interphase Enables Long Cycle Life Performance in Organic Cathodes for Potassium‐Ion Batteries. *Advanced Functional Materials* **2019,** *29* (5), 1807137.

41.   Zhang, J.; Wang, D.-W.; Lv, W.; Zhang, S.; Liang, Q.; Zheng, D.; Kang, F.; Yang, Q.-H., Achieving superb sodium storage performance on carbon anodes through an ether-derived solid electrolyte interphase. *Energy & Environmental Science* **2017,** *10* (1), 370-376.

42.   Tao, H.; Zhou, M.; Wang, R.; Wang, K.; Cheng, S.; Jiang, K., TiS$_2$ as an Advanced Conversion Electrode for Sodium-Ion Batteries with Ultra-High Capacity and Long-Cycle Life. *Advanced Science* **2018,** *5* (11), 1801021.

43.   Yang, H.; Xu, R.; Yao, Y.; Ye, S.; Zhou, X.; Yu, Y., Multicore-shell Bi@N-doped carbon nanospheres for high power density and long cycle life sodium-and potassium-ion anodes. *Advanced Functional Materials* **2019,** *29* (13), 1809195.

44.   Fan, X.; Gao, T.; Luo, C.; Wang, F.; Hu, J.; Wang, C., Superior reversible tin phosphide-carbon spheres for sodium ion battery anode. *Nano energy* **2017,** *38*, 350-357.

45.   Xu, K., Li-ion battery electrolytes. *Nature Energy* **2021,** *6* (7), 763-763.

46.   Ponrouch, A.; Marchante, E.; Courty, M.; Tarascon, J.-M.; Palacin, M. R., In search of an optimized electrolyte for Na-ion batteries. *Energy & Environmental Science* **2012,** *5* (9), 8572-8583.

47.   Eshetu, G. G.; Elia, G. A.; Armand, M.; Forsyth, M.; Komaba, S.; Rojo, T.; Passerini, S., Electrolytes and interphases in sodium-based rechargeable batteries: recent advances and perspectives. *Advanced Energy Materials* **2020,** *10* (20), 2000093.

48.   Morales, D.; Ruther, R. E.; Nanda, J.; Greenbaum, S., Ion transport and association study of glyme-based electrolytes with lithium and sodium salts. *Electrochimica Acta* **2019,** *304*, 239-245.

49.   Gao, Y.; Du, X.; Hou, Z.; Shen, X.; Mai, Y.-W.; Tarascon, J.-M.; Zhang, B., Unraveling the mechanical origin of stable solid electrolyte interphase. *Joule* **2021,** *5* (7), 1860-1872.

50.   Xie, H.; Kalisvaart, W. P.; Olsen, B. C.; Luber, E. J.; Mitlin, D.; Buriak, J. M., Sn-Bi-Sb alloys as anode materials for sodium ion batteries. *Journal of Materials Chemistry A* **2017,** *5* (20), 9661-9670.

51.   Eom, K.; Jung, J.; Lee, J. T.; Lair, V.; Joshi, T.; Lee, S. W.; Lin, Z.; Fuller, T. F., Improved stability of nano-Sn electrode with high-quality nano-SEI formation for lithium ion battery. *Nano Energy* **2015,** *12*, 314-321.

52.   Liu, Q.; Cresce, A.; Schroeder, M.; Xu, K.; Mu, D.; Wu, B.; Shi, L.; Wu, F., Insight on lithium metal anode interphasial chemistry: Reduction mechanism of cyclic ether solvent and SEI film formation. *Energy Storage Materials* **2019,** *17*, 366-373.

53.   Xu, K., Electrolytes and interphases in Li-ion batteries and beyond. *Chemical reviews* **2014,** *114* (23), 11503-11618.

54.   Cao, X.; Ren, X.; Zou, L.; Engelhard, M. H.; Huang, W.; Wang, H.; Matthews, B. E.; Lee, H.; Niu, C.; Arey, B. W., Monolithic solid-electrolyte interphases formed in fluorinated orthoformate-based electrolytes minimize Li depletion and pulverization. *Nature Energy* **2019,** *4* (9), 796-805.

55.   Yu, Z.; Wang, H.; Kong, X.; Huang, W.; Tsao, Y.; Mackanic, D. G.; Wang, K.; Wang, X.; Huang, W.; Choudhury, S.; Zheng, Y.; Amanchukwu, C. V.; Hung, S. T.; Ma, Y.; Lomeli, E. G.; Qin, J.; Cui, Y.; Bao, Z., Molecular design for electrolyte solvents enabling energy-dense and long-cycling lithium metal batteries. *Nature Energy* **2020,** *5* (7), 526-533.

56.   Aurbach, D., Review of selected electrode-solution interactions which determine the performance of Li and Li ion batteries. *Journal of Power Sources* **2000,** *89* (2), 206-218.

57.   Aurbach, D.; Granot, E., The study of electrolyte solutions based on solvents from the "glyme" family (linear polyethers) for secondary Li battery systems. *Electrochimica acta* **1997,** *42* (4), 697-718.

58.   Gelius, U.; Heden, P.; Hedman, J.; Lindberg, B.; Manne, R.; Nordberg, R.; Nordling, C.; Siegbahn, K., Molecular spectroscopy by means of ESCA III. Carbon compounds. *Physica Scripta* **1970,** *2* (1-2), 70.

59.   Muñoz-Márquez, M. A.; Zarrabeitia, M.; Castillo-Martínez, E.; Eguía-Barrio, A.; Rojo, T. f.; Casas-Cabanas, M., Composition and evolution of the solid-electrolyte interphase in $Na_2Ti_3O_7$ electrodes for Na-ion batteries: XPS and Auger parameter analysis. *ACS applied materials & interfaces* **2015,** *7* (14), 7801-7808.

60.   Ma, M.; Cai, H.; Xu, C.; Huang, R.; Wang, S.; Pan, H.; Hu, Y. S., Engineering Solid Electrolyte Interface at Nano-Scale for High-Performance Hard Carbon in Sodium-Ion Batteries. *Advanced Functional Materials* **2021**, 2100278.

61.   Gong, C.; Pu, S. D.; Gao, X.; Yang, S.; Liu, J.; Ning, Z.; Rees, G. J.; Capone, I.; Pi, L.; Liu, B., Revealing the Role of Fluoride-Rich Battery Electrode Interphases by Operando Transmission Electron Microscopy. *Advanced Energy Materials* **2021,** *11* (10), 2003118.

62.   Wang, Y.; Liu, F.; Fan, G.; Qiu, X.; Liu, J.; Yan, Z.; Zhang, K.; Cheng, F.; Chen, J., Electroless Formation of a Fluorinated Li/Na Hybrid Interphase for Robust Lithium Anodes. *Journal of the American Chemical Society* **2021,** *143* (7), 2829-2837.

63.   Zhang, X.; Hao, F.; Cao, Y.; Xie, Y.; Yuan, S.; Dong, X.; Xia, Y., Dendrite-Free and Long-Cycling Sodium Metal Batteries Enabled by Sodium-Ether Cointercalated Graphite Anode. *Advanced Functional Materials* **2021,** *31* (15), 2009778.

64.   Chen, J.; Fan, X.; Li, Q.; Yang, H.; Khoshi, M. R.; Xu, Y.; Hwang, S.; Chen, L.; Ji, X.; Yang, C., Electrolyte design for LiF-rich solid-electrolyte interfaces to enable high-performance microsized alloy anodes for batteries. *Nature Energy* **2020,** *5* (5), 386-397.

65.   Shin, H.; Park, J.; Han, S.; Sastry, A. M.; Lu, W., Component-/structure-dependent elasticity of solid electrolyte interphase layer in Li-ion batteries: experimental and computational studies. *Journal of Power Sources* **2015,** *277*, 169-179.